

9-25-2017

Phase Behavior of Binary and Polydisperse Suspensions of Compressible Microgels Controlled by Selective Particle Deswelling

A. Scotti

Paul Scherrer Institut

U. Gasser

Paul Scherrer Institut

E. S. Herman

Georgia Institute of Technology

Jun Han

Paul Scherrer Institut

A. Menzel

Paul Scherrer Institut

See next page for additional authors

Follow this and additional works at: http://digitalcommons.chapman.edu/sees_articles



Part of the [Other Chemistry Commons](#), [Physical Chemistry Commons](#), and the [Polymer Chemistry Commons](#)

Recommended Citation

A. Scotti, U. Gasser, E. S. Herman, J. Han, A. Menzel, L. A. Lyon, and A. Fernandez-Nieves, *Phys. Rev. E* **96**, 032609 (2017).
doi:10.1103/PhysRevE.96.032609

This Article is brought to you for free and open access by the Science and Technology Faculty Articles and Research at Chapman University Digital Commons. It has been accepted for inclusion in Biology, Chemistry, and Environmental Sciences Faculty Articles and Research by an authorized administrator of Chapman University Digital Commons. For more information, please contact laughtin@chapman.edu.

Phase Behavior of Binary and Polydisperse Suspensions of Compressible Microgels Controlled by Selective Particle Deswelling

Comments

This article was originally published in *Physical Review E*, volume 96r, in 2017. DOI: [10.1103/PhysRevE.96.032609](https://doi.org/10.1103/PhysRevE.96.032609)

Copyright

American Physical Society

Authors

A. Scotti, U. Gasser, E. S. Herman, Jun Han, A. Menzel, L. Andrew Lyon, and A. Fernandez-Nieves

Phase behavior of binary and polydisperse suspensions of compressible microgels controlled by selective particle deswelling

A. Scotti,^{1,2,*} U. Gasser,^{1,†} E. S. Herman,³ Jun Han,^{4,‡} A. Menzel,⁴ L. A. Lyon,⁵ and A. Fernandez-Nieves²

¹*Laboratory for Neutron Scattering and Imaging, Paul Scherrer Institut, 5232 Villigen, Switzerland*

²*School of Physics, Georgia Institute of Technology, Atlanta, Georgia 30332, USA*

³*School of Chemistry and Biochemistry, Georgia Institute of Technology, Atlanta, Georgia 30332, USA*

⁴*Laboratory for Macromolecules and Bioimaging, Paul Scherrer Institut, 5232 Villigen, Switzerland*

⁵*Schmid College of Science and Technology, Chapman University, Orange, California 92866, USA*

(Received 14 June 2017; published 25 September 2017)

We investigate the phase behavior of suspensions of poly(*N*-isopropylacrylamide) (pNIPAM) microgels with either bimodal or polydisperse size distribution. We observe a shift of the fluid-crystal transition to higher concentrations depending on the polydispersity or the fraction of large particles in suspension. Crystallization is observed up to polydispersities as high as 18.5%, and up to a number fraction of large particles of 29% in bidisperse suspensions. The crystal structure is random hexagonal close-packed as in monodisperse pNIPAM microgel suspensions. We explain our experimental results by considering the effect of bound counterions. Above a critical particle concentration, these cause deswelling of the largest microgels, which are the softest, changing the size distribution of the suspension and enabling crystal formation in conditions where incompressible particles would not crystallize.

DOI: [10.1103/PhysRevE.96.032609](https://doi.org/10.1103/PhysRevE.96.032609)

I. INTRODUCTION

A detailed understanding of the fluid to crystal transition and, more generally, of the phase behavior is of fundamental importance for the application of any material. Factors controlling this include thermodynamic variables, like temperature and pressure, and internal parameters of the material under consideration, like the presence of dopants or impurities, and polydispersity in size. Indeed, size polydispersity often limits or suppresses crystallization. In metal melts, the presence of point defects caused by a size mismatch of 15% suppresses crystallization [1], and in hard spheres, an important model system for condensed matter, crystallization is suppressed for polydispersities $>12\%$. Furthermore, the polydispersity in a monocrystal of hard spheres is not higher than 5.7%, as particle segregation occurs during crystallization [2–6]. Since size mismatch strongly limits the formation of crystals, it came as a big surprise that this limitation does not apply for soft, colloidal microgels. In this case, particles that were too large to fit in the crystal lattice formed by smaller particles spontaneously deswelled to fit in the crystal without causing point defects that would otherwise have prevented crystallization [7].

Microgels are cross-linked polymer particles immersed in a solvent, which can exist in a soft and swollen or in a stiff and deswollen state depending on external parameters like temperature [8,9], pH [10,11], and pressure [12–14]. The spontaneous deswelling of large microgels has been observed in aqueous suspensions of poly(*N*-isopropylacrylamide)

(pNIPAM) microgels; we have recently provided an explanation for the observed deswelling behavior [15]. Despite pNIPAM is an uncharged polymer, the pNIPAM microgels used in this work carry charged groups in their peripheral, fuzzy corona, which are due to the initiator employed in the synthesis, ammonium persulfate [APS, $(\text{NH}_4)_2\text{S}_2\text{O}_8$]; this is schematically illustrated in Fig. 1(a) with \ominus symbols. Once the microgels are in suspension, the ammonium counterions, NH_4^+ , that are weakly attracted to the microgel can escape and contribute to the suspension osmotic pressure [15–17]. Most counterions, however, remain bound to the particle [see Fig. 1(b)]. Interestingly, at sufficiently high microgel concentrations, the clouds of bound counterions overlap and eventually percolate through the system, as schematically illustrated in Fig. 1(c). At this point, the bound counterions are effectively free to explore the space outside the particles. This causes a strong increase in the suspension osmotic pressure that, in addition, produces an osmotic pressure difference, $\Delta\Pi$, between the inside and outside of the particles. If $\Delta\Pi$ exceeds the bulk modulus of the particles, then deswelling occurs. The softest particles deswell first, and more particles are affected as the concentration and hence the osmotic pressure difference increases.

In this paper, we study the effect of spontaneous deswelling on the phase behavior of pNIPAM suspensions with controlled polydispersity or bimodal size distribution. Varying the microgel concentration and either the polydispersity or the number ratio of large and small particles, we determine the phase behavior using structure factors obtained from small-angle x-ray scattering (SAXS) and visual inspection of the crystalline fraction in the suspension. With increasing microgel concentration, the largest particles in the suspension, which are also the softest, are observed to deswell before the smaller particles do. This implies a reduction in size polydispersity that enables crystallization under conditions that would suppress crystallization in other materials. Whether crystallization takes place depends on the stiffness of the particles and the initial

*Present address: Institute of Physical Chemistry, RWTH Aachen University, 52056 Aachen, Germany.

†Corresponding author: urs.gasser@psi.ch

‡Present address: Quanzhou Institute of Equipment Manufacturing, Haixi Institutes, Chinese Academy of Sciences, Quanzhou 362200, People's Republic of China.

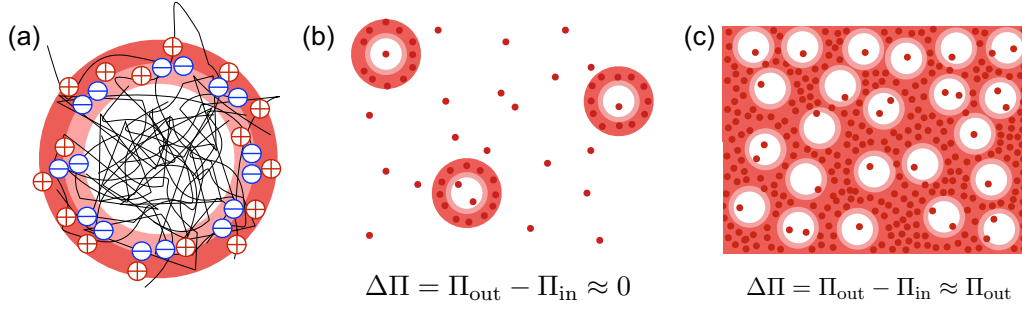


FIG. 1. (a) Microgel particle and its counterion cloud that extends towards the outside (dark red shell) and the inside (light red shell) of the particle. The fixed charges and the counterions are represented by \ominus and \oplus , respectively. (b) Dilute suspension where only a small fraction of the counterions (\bullet) can leave the particle due to thermal fluctuations. (c) Concentrated suspension with percolated counterion clouds. The bound counterions freely explore the volume between the microgels.

size distribution. For example, in bidisperse suspensions with a fixed size ratio of large and small particles, the freezing point increases with the number fraction of large particles. In contrast, for polydisperse suspensions with an approximately Gaussian size distribution, the freezing point does not depend as much on polydispersity. We observe crystallization up to a number fraction of large particles of 29% in the bidisperse case, and find an upper polydispersity limit for crystallization of polydisperse suspensions with approximately Gaussian size distributions of about 18.5%, which is considerably higher than the limit of 12% in hard spheres [2,3].

II. EXPERIMENTAL

A. Particle synthesis and samples

All pNIPAM microgels used in this study have been synthesized by precipitation polymerization [18,19]. *N*-isopropylacrylamide (NIPAM, 98 wt%) and *N,N'*-methylenebis(acrylamide) (BIS, 2 wt%) at a total concentration of 100 mM, together with sodium dodecyl sulfate (SDS), are dissolved in 995 ml of distilled, deionized water. The amount of SDS is varied from 0.50 mM to 1.25 mM to control the particle size [19]. The solution is initially filtered through a 0.2 μm Supor membrane filter into a 2 liter three-neck round bottom flask, heated to 70 $^{\circ}\text{C}$, and kept under a nitrogen atmosphere while continuously stirred. After 1 hr, the reaction is initiated by adding 5 ml of ammonium persulfate (1.0 mM). Therefore, the final suspension volume for the reaction is 1 l. The reaction takes place for 6 hr and is terminated by cooling to room temperature. Undesired aggregates are removed by filtering with a 0.8 μm Supor membrane filter, and the resulting particle suspension is purified using dialysis, with water being changed daily for 10 days, to remove the surfactant and purify the suspension. We note that SDS is an ionic surfactant. As a result, in addition to the NH_4^+ coming from the initiator, the solution will also contain counterions resulting from the ionization of SDS; these are Na^+ ions. Therefore, the microgel electric double layer is complex and will contain both NH_4^+ and Na^+ ions. Hence even if, for simplicity, we refer to NH_4^+ ions, it is to be understood that we more generally refer to the counterions, which could either be NH_4^+ or Na^+ ions. Finally, the particles are freeze-dried, and the resulting powder is used to prepare the samples.

To study the dependence of the phase behavior on polydispersity, particles have been synthesized with radii in the range from 71 to 192 nm, as listed in Table I. We refer to the samples as obtained from synthesis as s-samples. These have polydispersities between 7% and 12%, which are the lowest polydispersities in our study. Only the smallest particles, sample s21, show a higher polydispersity. In the synthesis, polydispersity is limited by controlling the size of the primary pNIPAM particles with the addition of SDS; this is more difficult to achieve when synthesizing smaller particles [20] and explains the larger polydispersity of sample s21.

Samples with a bimodal size distribution, named b-samples, are obtained by mixing two s-samples with different radii in ultrapure water with a resistivity of 18.2 $\text{M}\Omega \cdot \text{cm}$. The large and small particles have hydrodynamic radii in the range from $R_l = 182$ nm to 192 nm and from $R_s = 137$ nm to 146 nm, respectively, resulting in size ratios R_l/R_s between 1.30 and 1.37, as listed in Table II. An important quantity is the number fraction of the large microgels: $n_l = N_l/N_{\text{tot}} = N_l/(N_l + N_s)$, where N_l and N_s are the number of large and small particles in the suspension, respectively. With our b-samples, we cover the range $0.1\% \lesssim n_l \lesssim 80\%$, as shown in Table II. This allows a systematic study of the phase behavior as a function of n_l .

Samples with monomodal, Gaussian-like size distribution, and polydispersity $p > 12\%$ are realized by mixing from two up to five different s-samples and are listed in Table III. We refer to these samples with increased polydispersity as p-samples. Although they have a monomodal size distribution, they are composed of s-samples; for example, sample p11 is obtained by mixing samples s5, s16, and s19 at the mass fractions indicated in the third column of Table III. It is thus still useful to refer to the smallest and largest particles in the p-samples as we do in the b-samples; for sample p11, these are the particles from samples s19 and s16, respectively.

The polydispersity of our samples has been obtained using dynamic light scattering (DLS) and small-angle neutron and x-ray scattering (SANS and SAXS, respectively). The DLS correlation functions have been analyzed using a modified CONTIN method [21], which directly gives the size distribution of the microgel suspension and allows for a direct calculation of the polydispersity, $p = \sqrt{\langle R^2 \rangle - \langle R \rangle^2} / \langle R \rangle$, with $\langle \dots \rangle$ referring to the mean. For SANS and SAXS, the

TABLE I. Radii and polydispersities for the s-samples obtained from DLS using CONTIN, SANS, and SAXS. Also shown are conversion constants, k , to calculate the volume fraction, and the collapsed radii as obtained from viscometry. The errors of the SANS and SAXS results have been obtained from fits to the measured data using Eqs. (6) and (7). “–” indicates that the corresponding SAXS measurement was not performed.

Sample	DLS		SANS		SAXS		Viscometry	
	R_h (nm)	p (%)	R_{SANS} (nm)	σ_p (%)	R_{SAXS} (nm)	σ_p (%)	k	R_{coll} (nm)
s1	131.7 ± 0.8	11.6 ± 2.9	124 ± 4	11 ± 1	127 ± 3	10.2 ± 0.2	17.3 ± 0.3	47 ± 1
s2	139 ± 1	11 ± 3	133.2 ± 2	10.0 ± 0.5	133 ± 2	10.9 ± 0.4	16.9 ± 0.3	50.0 ± 0.6
s3	144 ± 2	11.4 ± 3.4	137 ± 5	10.1 ± 0.6	140 ± 1	10.8 ± 0.6	17.2 ± 0.5	51.5 ± 0.8
s4	139.5 ± 0.8	11.2 ± 3.2	120 ± 2	11.0 ± 0.4	–	–	20.6 ± 0.9	46.5 ± 0.2
s5	137 ± 1	10.4 ± 1.0	131 ± 5	10.1 ± 0.7	–	–	18.1 ± 0.6	48.5 ± 0.4
s6	143 ± 1	8.9 ± 1.1	132 ± 3	8.5 ± 0.8	133.8 ± 0.3	8.7 ± 0.1	19.0 ± 0.5	49.5 ± 0.9
s7	141 ± 1	10.2 ± 2.2	134 ± 3	10.8 ± 0.4	137.6 ± 0.5	10.7 ± 0.1	17.9 ± 0.3	49.8 ± 0.2
s8	140.4 ± 0.9	8.0 ± 2.3	135 ± 3	7.0 ± 0.4	–	–	17.9 ± 0.8	49.5 ± 0.9
s9	146 ± 1	7.1 ± 1.1	133 ± 2	8.1 ± 0.6	140 ± 2	8 ± 1	17.9 ± 0.4	51.5 ± 0.9
s10	142.9 ± 0.9	11 ± 3	137 ± 4	10.2 ± 0.4	138.4 ± 0.7	9.5 ± 0.8	17.3 ± 0.8	51.0 ± 0.6
s11	182 ± 2	9.8 ± 2.5	176 ± 4	11.6 ± 0.5	173 ± 4	10.3 ± 0.8	16.9 ± 0.1	65.5 ± 0.4
s12	185 ± 7	9.2 ± 1.6	180 ± 6	9.3 ± 0.6	180 ± 1	10.6 ± 0.4	19.2 ± 0.3	63.7 ± 0.7
s13	192 ± 2	9.0 ± 2.6	180 ± 6	10 ± 1	179.8 ± 0.4	9.6 ± 0.7	18.1 ± 0.7	67.5 ± 0.9
s14	187 ± 3	10.3 ± 1.4	180 ± 8	11 ± 2	181.4 ± 0.5	9.7 ± 0.6	18.0 ± 0.3	65.9 ± 0.7
s15	134.1 ± 0.9	7.8 ± 1.2	129 ± 3	9.1 ± 0.9	134.1 ± 2	9.6 ± 0.5	19.1 ± 0.7	46 ± 1
s16	167 ± 2	10.4 ± 1.8	158 ± 3	8.5 ± 0.9	–	–	20.0 ± 0.5	55.8 ± 0.6
s17	126 ± 1	10.4 ± 1.8	126 ± 2	10.8 ± 0.5	116.0 ± 0.6	10.6 ± 0.2	19.3 ± 0.3	43.3 ± 0.6
s18	170 ± 2	10.9 ± 2.6	158 ± 5	11 ± 1	158.5 ± 0.5	10 ± 1	20.3 ± 0.2	57.5 ± 0.4
s19	119 ± 1	8.5 ± 1.6	115 ± 4	10.1 ± 0.4	112 ± 1	10.1 ± 0.4	19.5 ± 0.8	41 ± 1
s20	113 ± 1	9.1 ± 1.6	111 ± 3	12 ± 1	–	–	16.2 ± 0.3	41.2 ± 0.8
s21	78.6 ± 0.6	17 ± 4	71 ± 2	22.2 ± 0.8	72.4 ± 0.5	20.7 ± 1	22 ± 1	25 ± 2

scattering curves of dilute samples were fitted with a model for the particle form factor that considers a Gaussian size distribution for the microgel core with associated polydispersity σ_p . The three techniques lead to consistent values for the polydispersity. The highest polydispersity reached for the p-samples is around 22%.

B. Generalized volume fraction

pNIPAM microgels are temperature sensitive and show a volume phase transition at $T \approx 32^\circ\text{C}$ [22,23]. In the work

reported here, we have kept the temperature in the range $18^\circ\text{C} < T < 21^\circ\text{C}$, where the microgels are in the fully swollen state. The suspension phase behavior is then controlled by the volume fraction, ϕ , which is hard to define for a microgel suspension, given that the particles can interpenetrate [24,25], compress [7,26], and change shape [27,28]. Hence, we use the generalized volume fraction, ζ :

$$\zeta = \frac{N_{\text{tot}} V}{V_{\text{tot}}} \approx \frac{m_{\text{pNIPAM}}}{m_{\text{tot}}} \frac{\rho_{\text{solvent}}}{\rho_{\text{pNIPAM}}} \frac{R^3}{R_{\text{coll}}^3}, \quad (1)$$

TABLE II. Composition, fraction of large particles, radii, and size ratios of large and small particles of the b-samples. “–” indicates that the corresponding SAXS measurement was not performed. The figure number is given in the last column for samples shown in Fig. 8.

Sample	Composition	n_1 (%)	DLS		SAXS		SANS		R_1/R_s	Fig.
			R_s (nm)	R_l (nm)	R_s (nm)	R_l (nm)	R_s (nm)	R_l (nm)		
b1	s6, s11	0.10 ± 0.07	143 ± 1	182 ± 2	133.8 ± 0.3	173 ± 4	132 ± 3	176 ± 4	1.33 ± 0.07	–
b2	s6, s11	0.4 ± 0.1	143 ± 1	182 ± 2	133.8 ± 0.3	173 ± 4	132 ± 3	176 ± 4	1.33 ± 0.07	–
b3	s6, s11	0.6 ± 0.1	143 ± 1	182 ± 2	133.8 ± 0.3	173 ± 4	132 ± 3	176 ± 4	1.33 ± 0.07	–
b4	s5, s11	1.4 ± 0.1	137 ± 1	182 ± 2	–	173 ± 4	131 ± 5	176 ± 4	1.34 ± 0.09	–
b5	s7, s11	2.3 ± 0.2	141 ± 1	182 ± 2	137.6 ± 0.5	173 ± 4	133 ± 4	176 ± 4	1.32 ± 0.08	–
b6	s7, s14	2.6 ± 0.2	141 ± 1	187 ± 3	137.6 ± 0.5	181.4 ± 0.5	133 ± 4	180 ± 8	1.35 ± 0.07	–
b7	s5, s13	4.7 ± 0.5	137 ± 1	192 ± 2	–	179.8 ± 0.4	131 ± 5	180 ± 6	1.37 ± 0.09	8(a)
b8	s8, s11	6.6 ± 0.7	140.4 ± 0.9	182 ± 2	–	173 ± 4	135 ± 3	176 ± 4	1.30 ± 0.05	–
b9	s7, s12	10.1 ± 0.9	141 ± 1	185 ± 7	137.6 ± 0.5	180 ± 1	133 ± 4	180 ± 8	1.35 ± 0.07	–
b10	s7, s11	18 ± 2	141 ± 1	182 ± 2	137.6 ± 0.5	173 ± 4	133 ± 4	176 ± 4	1.32 ± 0.08	8(b)
b11	s10, s12	29 ± 3	142.9 ± 0.9	185 ± 7	138.4 ± 0.7	180 ± 1	137 ± 4	180 ± 8	1.36 ± 0.09	8(c)
b12	s9, s13	38 ± 4	146 ± 1	192 ± 2	140 ± 2	179.8 ± 0.4	133 ± 2	180 ± 6	1.35 ± 0.07	8(d)
b13	s9, s13	79 ± 8	146 ± 1	192 ± 2	140 ± 2	179.8 ± 0.4	133 ± 2	180 ± 6	1.33 ± 0.08	8(e), 8(f)

TABLE III. Composition, mass fraction of the components, and radii and polydispersities of the p-samples obtained from DLS using CONTIN, SANS, and SAXS. The errors of the SANS and SAXS results have been obtained from fits to the measured data using Eqs. (6) and (7). The figure number is given in the last column for samples shown in Fig. 9.

Sample	Composition	$m_{\text{poly}} (\%)$	DLS		SANS		SAXS		Fig.
			R_h (nm)	p (%)	R_{SANS} (nm)	σ_p (%)	R_{SAXS} (nm)	σ_p (%)	
p1	s10, s15	$66.13 \pm 0.02, 33.87 \pm 0.02$	142 ± 7	11 ± 3	131 ± 1	11.0 ± 0.6	132.1 ± 0.3	11.0 ± 0.3	–
p2	s7, s19	$54.96 \pm 0.04, 45.04 \pm 0.04$	134 ± 4	10.8 ± 3.1	127.9 ± 0.9	11.8 ± 0.4	132.6 ± 0.5	11.1 ± 0.1	–
p3	s9, s20	$50.94 \pm 0.04, 49.06 \pm 0.04$	132 ± 9	11.1 ± 4.8	130.2 ± 0.9	13.1 ± 0.4	131.7 ± 0.3	14 ± 2	–
p4	s15, s18	$50.01 \pm 0.04, 49.99 \pm 0.04$	147 ± 7	13.9 ± 4.3	136 ± 1	14.1 ± 0.6	135 ± 2	14.0 ± 0.8	9(a)
p5	s16, s17	$55.44 \pm 0.04, 44.56 \pm 0.04$	143 ± 7	13.3 ± 2.7	130.8 ± 0.9	12.9 ± 0.4	132 ± 2	13.5 ± 0.8	9(d)
p6	s15, s18	$53.00 \pm 0.04, 47.00 \pm 0.04$	150 ± 7	16.4 ± 4.1	139 ± 1	16.8 ± 0.7	140 ± 2	16.2 ± 0.9	–
p7	s9, s20	$35.18 \pm 0.03, 64.82 \pm 0.05$	139 ± 14	14.4 ± 1.7	125 ± 1	14.2 ± 0.5	128.7 ± 0.2	14.9 ± 0.1	9(b), 9(e)
p8	s4, s20	$67.12 \pm 0.05, 32.88 \pm 0.03$	137 ± 6	13.7 ± 2.2	135 ± 1	14.1 ± 0.4	136 ± 2	14.7 ± 0.8	9(c)
p9	s16, s17	$50.18 \pm 0.04, 49.82 \pm 0.04$	152 ± 13	15.0 ± 1.9	136 ± 1	15.4 ± 0.6	137 ± 1	16.2 ± 0.4	–
p10	s1, s16	$50.25 \pm 0.04, 49.75 \pm 0.04$	145 ± 16	16.5 ± 1.4	138 ± 2	17 ± 1	145 ± 2	18.5 ± 0.9	–
p11	s5, s16, s19	$60.20 \pm 0.05, 14.88 \pm 0.02,$ 24.92 ± 0.03	138 ± 10	17.2 ± 1.6	128 ± 1	18.3 ± 0.7	126 ± 4	17 ± 2	–
p12	s7, s18, s20	$50.96 \pm 0.05, 38.79 \pm 0.04,$ 10.25 ± 0.03	148 ± 14	16.6 ± 1.3	125 ± 2	16.6 ± 0.8	129 ± 2	17 ± 1	9(f)
p13	s4, s16, s17, s20, s21	$22.98 \pm 0.06, 28.10 \pm 0.02,$ $31.22 \pm 0.05, 15.27 \pm 0.05,$ 2.43 ± 0.09	140 ± 6	20 ± 4	128 ± 6	19 ± 4	122 ± 1	22 ± 1	–
p14	s2, s16, s17, s20	$40.18 \pm 0.04, 23.04 \pm 0.06,$ $8.41 \pm 0.06, 28.37 \pm 0.05$	127 ± 4	19 ± 5	132 ± 5	20 ± 4	123 ± 3	21.4 ± 0.7	–

where $V = 4\pi R^3/3$, V_{tot} , m_{pNIPAM} , and m_{tot} are the microgel particle and sample volumes, and the masses of pNIPAM in suspension and the total sample, respectively. The quantity ρ_{solvent} is the density of the solvent, which in our experiments is either water or heavy water, and $\rho_{\text{pNIPAM}} = 1.269 \text{ g/cm}^3$ [29] is the density of dry pNIPAM. We assume the densities of the suspension and the solvent are equal, as the polymer concentration is always lower than 5 wt%. The symbols R and R_{coll} represent the particle radii in the swollen and collapsed state, respectively. The latter is the radius of the dry particle, which is smaller than the particle radius in the deswollen state, where the particle still contains some solvent [30]. Note that ζ agrees with ϕ for dilute samples with particles in the fully swollen state. However, since microgels can compress and deform, ζ can exceed 1, despite the volume fraction is limited to $\phi \leq 1$.

Since b- and p-samples are prepared by mixing the powder of different s-samples, their generalized volume fraction is determined as the sum of the generalized volume fractions of the involved s-samples: $\zeta_{\text{tot}} = \sum_i \zeta_i$, where ζ_i is computed using Eq. (1) for the i th s-sample, always using the same total sample volume.

C. Dynamic light scattering

To obtain ζ using Eq. (1), the radius of the swollen particle is needed, which we obtain from DLS measurements. The instrument used is a LS-Instruments 3D DLS-Pro spectrometer equipped with a vertically polarized He-Ne laser of vacuum wavelength $\lambda_0 = 632.8 \text{ nm}$. All measurements were taken in water, which has a refractive index $n(\lambda_0) = 1.33$ and a viscosity $\eta_{\text{H}_2\text{O}} = 1.002 \times 10^{-3} \text{ Pa} \cdot \text{s}$ at temperature $T = (20.0 \pm 0.5)^\circ\text{C}$. The samples for DLS are dilute, $\zeta \approx 0.02$,

such that the interaction between particles can be neglected. We analyze the DLS data using both cumulants [31,32] and a modified CONTIN method [21], which uses the original CONTIN algorithm [33,34] together with the L -curve criterion to choose the regularizer [21]. In this way, we can obtain the hydrodynamic-radius distribution and, from it, the polydispersity p . For the s-samples, we obtain $7\% < p < 12\%$; this agrees with sedimentation time measurements [35] and SANS measurements [36] of microgels synthesized with a similar protocol. The values of the hydrodynamic radii and the polydispersities obtained by means of the CONTIN analysis are reported in Tables I and III for s- and p-samples, respectively. The values and their associated errors are the mean and the standard deviation of 10 independent measurements taken at scattering angles between 20° and 140° .

D. Viscometry

We determine the collapsed radius in Eq. (1) from viscometry data obtained with dilute samples and the swollen hydrodynamic radius [30]. The suspension viscosity, η , is measured using an Ubbelohde tube immersed in a water bath with a fixed temperature of $T = (22.00 \pm 0.01)^\circ\text{C}$ [35,37]. Series of five or six suspensions with polymer mass fractions $c = m_{\text{pNIPAM}}/m_{\text{tot}}$ between 10^{-3} and 4×10^{-3} are measured for each s-sample, as done in earlier work [22,30]. From the Einstein-Batchelor relation [38], we know that the relative viscosity, $\eta_r = \eta/\eta_{\text{H}_2\text{O}}$, depends on ζ as [17,22]

$$\begin{aligned} \eta_r &= 1 + 2.5\zeta + 5.9\zeta^2 \\ &= 1 + 2.5(kc) + 5.9(kc)^2. \end{aligned} \quad (2)$$

Here we have used Eq. (1) to write $\zeta = kc$ with $k = (\rho_{\text{solvent}} R^3)/(\rho_{\text{pNIPAM}} R_{\text{coll}}^3)$ the conversion constant relating ζ

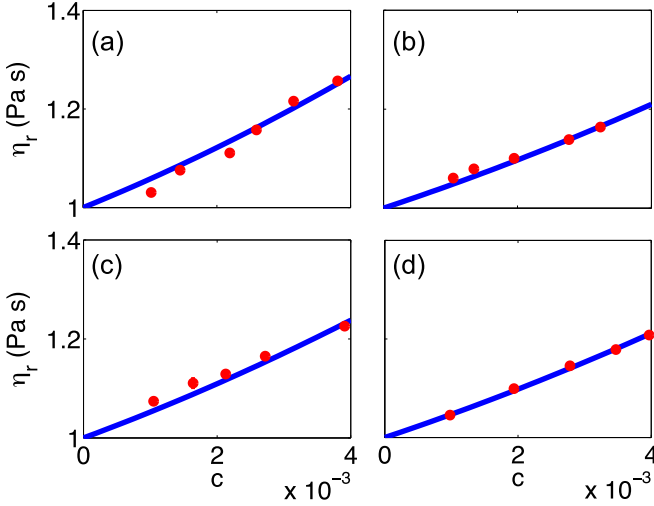


FIG. 2. Relative viscosity η_r as a function of microgel concentration given by the polymer mass fraction c for (a) s21, $R_h = (78.6 \pm 0.6)$ nm, $m_p = (0.9 \pm 0.1) \times 10^{-19}$ kg; (b) s2, $R_h = (139 \pm 1)$ nm, $m_p = (6.3 \pm 0.6) \times 10^{-19}$ kg; (c) s16, $R_h = (167 \pm 2)$ nm, $m_p = (9.2 \pm 0.7) \times 10^{-19}$ kg; (d) s11, $R_h = (182 \pm 2)$ nm, $m_p = (14 \pm 2) \times 10^{-19}$ kg. The experimental data (●) are fitted with Eq. (2) (curves).

and c . This constant k is obtained by fitting the measured $\eta_r(c)$ data with Eq. (2), as shown in Fig. 2. We then recall that $k = \zeta/c \approx (V_p \rho_{\text{solvent}})/m_p$, where m_p is the polymer mass of one particle and $V_p = 4\pi R_h^3/3$ its volume in the swollen state, which we obtain using the hydrodynamic radius. We then see that $m_p = (V_p \rho_{\text{solvent}})/k$ and thus

$$R_{\text{coll}} = \left(\frac{3}{4\pi} \frac{m_p}{\rho_{\text{pNIPAM}}} \right)^{1/3}. \quad (3)$$

The values of the conversion constant and the collapsed radii obtained from the analysis of the viscometry data are reported in Table I. Note that k has similar values for all s-samples, since all particles were synthesized with the same protocol and the same amount of crosslinker. This further indicates that all particles have comparable swelling ratio. Note also that we use m_p to calculate the number of particles in b- and p-samples: $N_i = m_i/m_{p,i}$, where $m_{p,i}$ and m_i refer to the polymer mass per particle and the total polymer mass of the i th s-sample used.

E. Form factors from small-angle neutron and x-ray scattering

The determination of the size polydispersity is of fundamental importance in this work, since we are interested in its effect on the phase behavior and, in particular, on crystallization. Therefore, we use SANS and SAXS as additional and independent tools to measure polydispersity. These methods also allow probing the internal structure of our microgels. During the synthesis, the crosslinker reacts faster than the NIPAM monomer, and, therefore, pNIPAM microgels have a more crosslinked spherical core with a denser polymer concentration compared to the surrounding softer, fuzzy shell. This gives the microgel its characteristic core-shell structure. We use a widely accepted model for the particle

form factor [9,36], which assumes a spherical core with radius R_c surrounded by a fuzzy shell with a decreasing polymer density. The fuzzy shell is obtained by convoluting the core with a Gaussian with standard deviation σ_s . The width of the shell is $2\sigma_s$, and the total radius of the particle is $R_c + 2\sigma_s$. In reciprocal space, the resultant form factor $P_1(q)$ is given by

$$P_1(R_c, q) = \left[\frac{3(\sin q R_c - q R_c \cos q R_c)}{(q R_c)^3} \right] \times \exp \left\{ -\frac{(\sigma_s q)^2}{2} \right\}. \quad (4)$$

Size polydispersity is taken into account assuming a Gaussian distribution for the core radius with standard deviation $\sigma_p \cdot \langle R_c \rangle$:

$$D(R_c) = \frac{1}{\sqrt{2\pi} \sigma_p \langle R_c \rangle} \exp \left[-\frac{(R_c - \langle R_c \rangle)^2}{2(\sigma_p \langle R_c \rangle)^2} \right], \quad (5)$$

where $\langle R_c \rangle$ and σ_p are the mean core radius and the relative distribution width, respectively.

For $q \gtrsim \pi/\sigma_s$, inhomogeneities within the particle make a measurable contribution to the scattering signal. This contribution is considered by adding a Lorentzian term to the scattered intensity, $I_{\text{chain}}(q) = I_{\text{chain}}(0)/[1 + (\xi q)^2]$, where ξ and $I_{\text{chain}}(0)$ are a correlation length related to the mesh size of the polymer network and the zero- q scattered intensity associated to this contribution, respectively [39–41]. With this, the model for the form factor of the particle becomes

$$P(q) = \frac{1}{\langle V^2 \rangle} \int_0^\infty dR_c D(R_c) V^2(R_c) P_1(R_c, q) + I_{\text{chain}}(q) + B \quad (6)$$

with $V(R_c) = 4\pi R_c^3/3$ the volume of the core and $\langle V^2 \rangle = \int_0^\infty dR_c V^2(R_c) D(R_c)$ the average squared core volume. The constant B accounts for the background due to incoherent scattering. Finally, we consider the instrument resolution by convoluting $P(q)$ with a Gaussian [42]:

$$P_s(q) = \frac{1}{\sqrt{2\pi} \sigma_r(q)} \int_0^\infty dq' \exp \left[-\frac{(q - q')^2}{2\sigma_r^2(q)} \right] P(q'), \quad (7)$$

where $\sigma_r^2(q)$ is the q -dependent variance with contributions due to the wavelength resolution, the geometrical resolution, and the downward-shift of the neutron beam due to gravity [43].

SANS measurements were performed at SINQ, Paul Scherrer Institut (Villigen, Switzerland), on the instruments SANS-I and SANS-II. We have covered the q -range of interest using two configurations: sample-detector distance $d_{\text{sd}} = 18$ m with wavelength $\lambda = 0.8$ nm and $d_{\text{sd}} = 4.5$ m with $\lambda = 0.8$ nm on SANS-I, and $d_{\text{sd}} = 6$ m with $\lambda = 1.05$ nm and $d_{\text{sd}} = 3$ m with $\lambda = 0.53$ nm on SANS-II. Both instruments are equipped with ^3He detectors with 128×128 pixels and pixel sizes of 7.5 mm and 4.3 mm, respectively. The temperature was fixed to (18.0 ± 0.5) °C for all SANS measurements. The form factors are measured using dilute samples with $\zeta \approx 0.08$, such that the structure factor $S(q) \approx 1$ and $P(q)$ can be measured directly.

Form factors were also measured using SAXS on the cSAXS beamline of the Swiss Light Source, Paul Scherrer Institut (Villigen, Switzerland). The instrument was set up

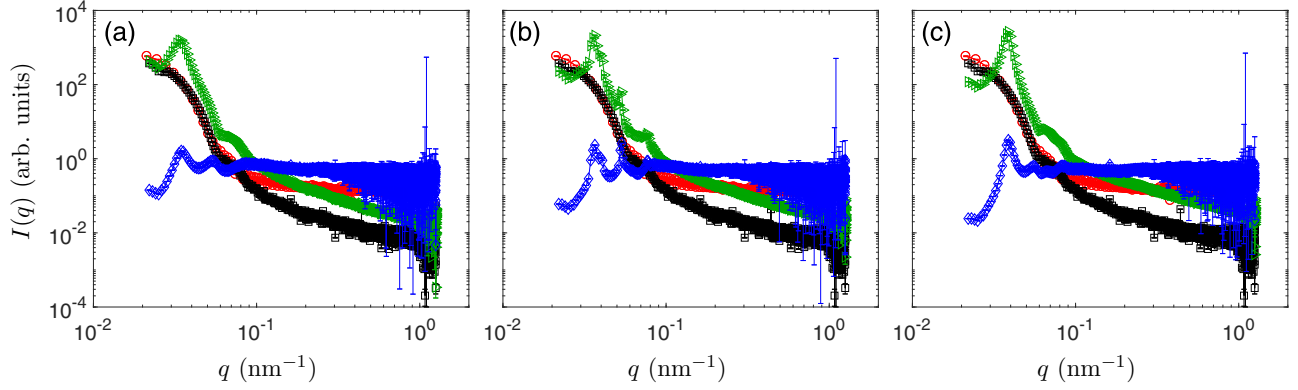


FIG. 3. Scattered intensity (\triangleright) and structure factor (\diamond) of sample s2 in (a) the fluid state at $\zeta = 0.51 \pm 0.01$, (b) the crystalline state at $\zeta = 0.64 \pm 0.02$, and (c) the disordered solid state at $\zeta = 0.82 \pm 0.02$. The form factors measured using SANS (\circ) at $\zeta = 0.08 \pm 0.01$ and SAXS (\square) at $\zeta = 0.06 \pm 0.01$ are shown in each panel.

with wavelength $\lambda = 0.145$ nm and wavelength resolution $\Delta\lambda/\lambda \approx 0.0002$. The sample-detector distance was $d_{sd} = 7.12$ m. The beam was collimated to illuminate an area of about $200 \times 200 \mu\text{m}^2$ on the sample. The 2D detector has 1475×1679 pixels and a pixel size of $172 \mu\text{m}$ [44].

As an example, the particle form factors obtained from SANS (\circ) and SAXS (\square) for sample s2 are shown in Fig. 3. Both curves can be described with the form factor model in Eq. (6). Note, the SANS data have a higher background than the SAXS data, which is mostly due to incoherent scattering from hydrogen.

From the analysis of the SANS and SAXS measurements, we see that (1) R_h is larger than both R_{SANS} and R_{SAXS} (see Tables I, II, and III); this is likely because small-angle scattering techniques are less sensitive to the dangling polymer chains at the particle periphery. (2) Polydispersities determined using the three different techniques all agree within experimental error.

F. Structure factors from small-angle x-ray scattering

We measure the suspension structure factor using SAXS to explore the phase behavior and the behavior of the large particles in fluid, crystalline, and glassy samples with either bimodal or polydisperse size distribution. The q -resolution on cSAXS allows resolving Bragg spots of single crystals in the scattering volume [45]. We prepare samples in quartz capillaries with a diameter of (1.0 ± 0.1) mm, and take measurements at 10 different points along the capillaries. At each point, we take a series of 10 measurements of 0.1 s each. For the analysis, only the data of the first 0.4 s are used to avoid artifacts due to x-ray damage or local heating. The temperature is fixed at $(18.0 \pm 0.5)^\circ\text{C}$.

At high concentrations, the scattered intensity exhibits oscillations due to the form factor and the structure of the microgel suspension, as shown with \triangleright symbols in Fig. 3. We obtain approximate structure factors from the SAXS data by dividing the scattered intensity by the form factor: $S(q) = I(q)/P(q)$; these are shown with \diamond symbols in all panels of Fig. 3. We see that the structure factor peaks are broad in fluid [Fig. 3(a)] and glassy samples [Fig. 3(c)], while there are sharper peaks in crystalline samples [Fig. 3(b)], which are due

to Bragg reflections and Bragg rods as explained in Sec. III D. The position of the first peak in $S(q)$, q_{peak} , is directly related to the nearest-neighbor distance: $d_{nn} = 2\pi/q_{\text{peak}}$. We emphasize that using a form factor, measured with a dilute sample, for suspensions at high ζ only allows obtaining an approximate structure factor. However, the error in the peak positions of $S(q)$ that results from doing this is small. From direct form factor measurements in highly concentrated pNIPAM suspensions using SANS with contrast matching [15], we know how the form factor changes up to $\zeta \approx 1.2$ and estimate that the position of the first peak in $S(q)$ at $\zeta \approx 0.8$ is displaced by only $\leq 0.0004 \text{ nm}^{-1}$ when we use a form factor obtained from a dilute suspension. This results in an error in d_{nn} of less than 2%.

III. RESULTS AND DISCUSSION

A. Phase behavior

To obtain an overview of the phase behavior of s-, b-, and p-samples, we prepared 10 to 16 suspensions at different concentrations for each sample, covering the freezing and melting points. All suspensions were kept at a fixed temperature of $T = (18.5 \pm 0.5)^\circ\text{C}$, and all show a qualitatively similar phase behavior. An example is shown in Fig. 4. Samples are fluid for concentrations below the freezing point, ζ_f , and show fluid-crystal coexistence from ζ_f up to the melting point, ζ_m . With further increase in concentration, the samples are fully crystalline or form a disordered, glassy phase. The crystalline samples show Bragg scattering in the

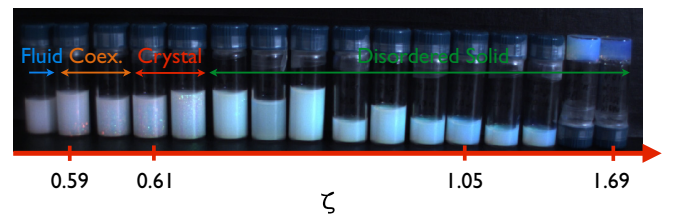


FIG. 4. Concentration series of sample s3 showing, with increasing ζ , the fluid, fluid-crystal coexistence, fully crystalline, and glassy state. In crystalline samples, the iridescence due to Bragg peaks is visible.

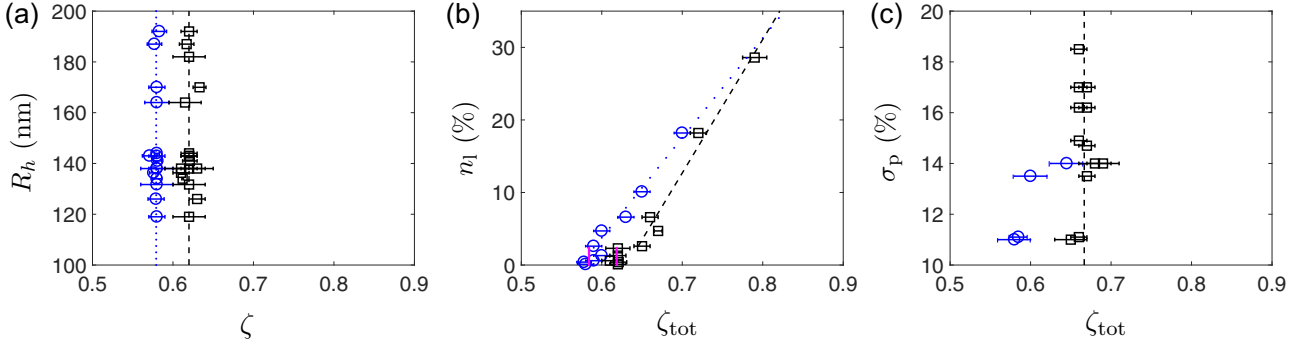


FIG. 5. Freezing (\circ) and melting (\square) points observed in (a) s-samples with particle radii in the range from 110 nm to 200 nm, (b) b-samples with varying fraction of large particles, n_1 , and (c) p-samples with polydispersities between 11% and 18.5%. The behavior of the freezing and melting points is highlighted by the dotted blue and dashed black lines, respectively. The magenta lines in (b) represent the freezing and melting lines for $n_1 \lesssim 2.5\%$. All phase behavior data are taken at $T = (18.3 \pm 0.5)^\circ\text{C}$.

visible spectrum and, therefore, the freezing point, ζ_f , and the melting point, ζ_m , have been identified by visual inspection of the samples. The s-samples have similar ζ_f and ζ_m , as shown in Fig. 5(a). By averaging the values for all samples, which have polydispersities $7\% < p < 12\%$, we obtain $\zeta_f = 0.58 \pm 0.02$ and $\zeta_m = 0.62 \pm 0.03$. The freezing and melting points agree with those found in other studies of pNIPAM microgels, where $0.56 \leq \zeta_f \leq 0.59$ and $\zeta_m = 0.61$ [22,46]; these values are higher than in the hard-sphere system, where $\phi_f = 0.494$ and $\phi_m = 0.545$ [47,48]. The s-samples show the fastest crystallization of all our samples, with crystals typically forming within 2 days.

Like the s-samples, the bidisperse b-samples, kept at the same temperature, also change from fluid to partially crystalline, to fully crystalline, and then to a disordered solid state, with increasing concentration. From visual inspection of the samples, we find the phase behavior shown in Fig. 5(b). We recognize that (1) for $n_1 \lesssim 2.5\%$, the freezing and melting points (magenta lines) agree with those of the s-samples shown in Fig. 5(a); (2) for $n_1 \gtrsim 2.5\%$, ζ_f and ζ_m shift to higher ζ with increasing n_1 ; (3) crystals are not observed for $n_1 \gtrsim 30\%$. Hence, for $n_1 \gtrsim 2.5\%$, the presence of the large particles causes an increase in ζ_f and ζ_m and plays a role in the narrowing and disappearance of the coexistence region.

The phase behavior of the polydisperse p-samples also differs from that of the s-samples. As shown in Fig. 5(c), we find that (1) for $\sigma_p < 14\%$, $\zeta_f = 0.58 \pm 0.02$ and $\zeta_m = 0.65 \pm 0.03$, consistent with the phase behavior of the s-samples. (2) In the range $14\% \lesssim \sigma_p \lesssim 15\%$, ζ_m remains constant at 0.68 ± 0.02 within the accuracy of our measurements, while the polydispersity has a strong effect on the freezing point, which increases to 0.65 ± 0.02 . (3) For $\sigma_p > 15\%$, we do not observe coexistence of fluid and crystal with our ζ resolution. (4) Finally, for $\sigma_p > 18.5\%$, crystallization is suppressed, a value considerably higher than the 12% polydispersity limit for hard spheres [1,2,49].

The phase behavior illustrated in Figs. 5(b) and 5(c) indicates that both n_1 and σ_p influence the freezing and melting points with respect to the s-samples shown in Fig. 5(a). Comparing the phase behavior of p- and b-samples, we find that, in the b-samples, both ζ_f and ζ_m strongly depend on n_1 ,

while for the p-samples ζ_m remains virtually unchanged and ζ_f is shifted very close to ζ_m , as σ_p is increased.

The crystallization time of the b- and p-samples is considerably longer than that of the s-samples: Crystals typically form within 2 wk. In hard spheres, an increased polydispersity is also found to strongly delay crystallization [4,5,50,51].

B. Microgel deswelling in concentrated suspensions

The swelling of a neutral microgel particle is determined by the interplay between the polymer-solvent mixing and the elasticity of the polymer network [52]. These two contributions are expressed in terms of osmotic pressures, Π_{mix} and Π_{el} , respectively. The equilibrium size of the microgel corresponds to having a zero osmotic pressure difference between the inside and the outside of the particle: $\Delta\Pi = \Pi_{\text{mix}} + \Pi_{\text{el}} - \Pi_{\text{out}} = 0$ [30], where Π_{out} is the osmotic pressure outside the microgel. Importantly, although pNIPAM microgels are neutral, they possess peripheric charges due to the initiator employed in the synthesis. Due to the electrostatic attraction between these fixed charges and the counterions, the microgel is surrounded by a counterion cloud. Within this cloud, there are counterions that are attracted with a strength larger than $k_B T$ and are thus bound to the particle. However, there are also counterions that are attracted with a strength comparable to or lower than $k_B T$; these are able to leave the particle due to the entropic gain associated with doing so. Note that the counterion cloud extends both inside and outside the particle. In Fig. 1(a) the charges at the periphery of the particle and the counterions are represented by \ominus and \oplus , respectively, while the microgel is represented by the inner white area and the light red shell.

Figure 1(b) illustrates the situation in a dilute sample, where the free counterions (\bullet outside the red clouds) set the osmotic pressure of the suspension [16,17,53]; they are essentially free to explore the inside as well as the outside of the microgel particles. Therefore, they do not give rise to a significant osmotic pressure difference between the inside and outside of the particles and cause no particle deswelling. When ζ is increased, however, the clouds of bound counterions start to overlap to eventually percolate through the sample, as illustrated in Fig. 1(c). At this point, the bound counterions become effectively free to explore all the volume outside the microgels and contribute to the osmotic pressure of the

suspension. This increase in Π_{out} is not compensated by a pressure increase inside the particles, as the electrostatic potential there is too high for the ions in the cloud of bound counterions to appreciably populate this region. This effect is observed in Monte Carlo simulations of a microgel modeled as a charged spherical surface surrounded by mobile counterions, see supporting information in Ref. [15]. At volume fractions $\gtrsim 0.5$, the electrostatic potential in the space between neighboring microgel particles was found to be lower than in the center of a particle as a result of the proximity of other particles. Hence, at a critical generalized volume fraction, if the osmotic pressure difference between the inside and the outside of the particle becomes larger than the bulk modulus of the microgel particle, the microgels appreciably deswell. We note that, depending on the thickness of the cloud of bound counterions, the percolation of the counterion clouds can occur below random close packing, $\phi_{\text{rcp}} \approx 0.64$. Therefore, the critical generalized volume fraction may be reached for ζ below or above ϕ_{rcp} , depending on the bulk modulus of the microgels and the amount of peripheral charge they have.

To determine the limiting concentration for the percolation of counterion clouds, we think of effective microgel particles composed of the microgel itself and the cloud of bound counterions at its periphery [15]. The radius of this effective particle is $R^{\text{eff}} = R + \Delta r$, where R is the radius of the microgel and Δr is the width of the counterion cloud outside the particle. This effective particle is sketched in Fig. 1(a); it consists of the inner white and the light- and dark-red volumes. To explain the behavior of samples with bimodal size distribution or polydispersity larger than 12%, we define the effective generalized volume fraction of the small effective particles in their accessible volume as $\zeta_s^{\text{eff}} = (R_s^{\text{eff}}/R_s)^3 \zeta_s / (1 - \phi_l)$, where we take into account that the small particles cannot access the volume taken by the large particles; ϕ_l represents the volume fraction taken by the large particles. We expect the counterion clouds to percolate, when the effective small particles fill all available space at $\zeta_s^{\text{eff}} \approx 1$. Consequently, particle deswelling is expected for $\zeta_s^{\text{eff}} \gtrsim 1$, provided $\Delta\Pi$ exceeds the microgel bulk modulus.

Furthermore, small particles are more rigid than large ones, when both are synthesized following the same protocol, which is the case in our work. The size of the microgel particles is controlled by the amount of SDS added, as it helps stabilize the pNIPAM particles at a definite size, preventing any subsequent growth [19]. Since particle growth is stopped earlier for small particles, the crosslinker concentration decays less from the center towards the periphery than in larger particles. It follows that larger particles have a softer periphery than smaller ones, and, therefore, in the swollen state, small particles have a higher bulk modulus than large particles. When the osmotic pressure in a polydisperse suspension is increased, the large particles deswell first [7, 15]. This reduces the size mismatch of small and large particles and can allow the suspension to crystallize.

C. Effect of particle deswelling on the phase behavior

To understand the shift of ζ_f and ζ_m observed in the b-samples [see Fig. 5(b)], we consider particle deswelling. In particular, we look at the size distribution of b-samples.

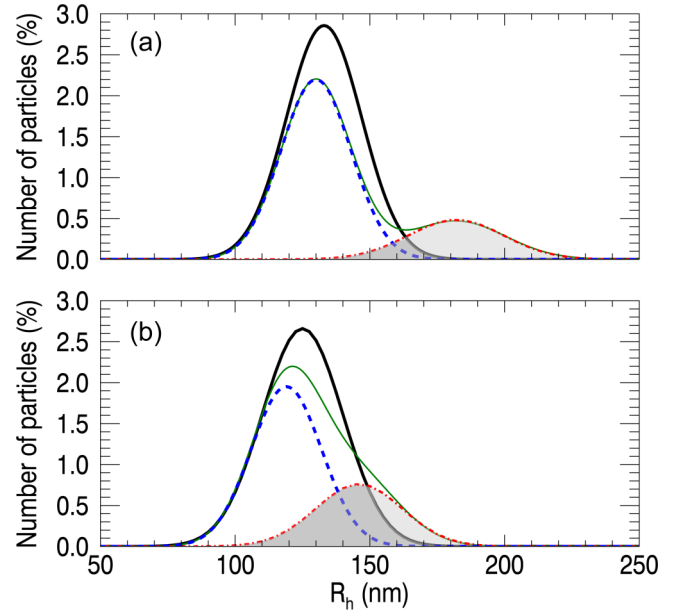


FIG. 6. Representation of the size distribution of (a) a b-sample with $n_1 = 10\%$ and (b) a p-sample with $p = 15\%$ with all particles fully swollen (thin green curve) and with large particles deswollen (thick black curve). The blue dashed curve and red dash-dotted curve show the size distributions of the involved small and large s-samples, respectively. The light gray areas highlight the fraction of large particles that deswell, whereas the dark gray areas represent the fraction of large particles that cooperates with the small ones in the deswelling mechanism.

Figure 6(a) is a representation using Gaussian size distributions and the experimental hydrodynamic radii and polydispersities of the large and small particles involved in the b-samples. The fraction of large microgels that needs to be deswollen to reduce the size mismatch and to allow for crystallization is indicated by the light gray area, as in this case, the size distribution of the suspension after the compression of the large particles (thick black curve) has an average size close to the size of the small particles (blue dashed curve). In samples with higher n_1 , the deswelling of the large particles occurs at a higher ζ , because a larger number of large particles needs to be compressed and, therefore, a larger volume becomes free. This implies that a higher concentration of small particles is needed to maintain the percolation of the counterion clouds and the osmotic pressure difference enabling the deswelling of the large particles. Therefore, the freezing point shifts to higher ζ_{tot} when n_1 increases, as shown in Fig. 7(a) with blue dots. The direct connection between crystallization and particle deswelling is apparent from looking at the values of ζ_s^{eff} for each ζ_f . In contrast to the behavior of ζ_f , ζ_s^{eff} does not depend on n_1 and is constant and equal to $\zeta_s^{\text{eff}} = 1.13 \pm 0.07$ for all n_1 , as shown with black squares in Fig. 7(a). The observed constancy of ζ_s^{eff} and the fact that $\zeta_s^{\text{eff}} > 1$ at freezing agrees with our expectations and reflects the fact that, before crystallization can start, the large particles have to be compressed to a size close to the size of the small particles.

While ζ_f strongly depends on n_1 in the b-samples, the influence of polydispersity in the p-samples is less pronounced. The freezing point does not appreciably depend on ζ_{tot}

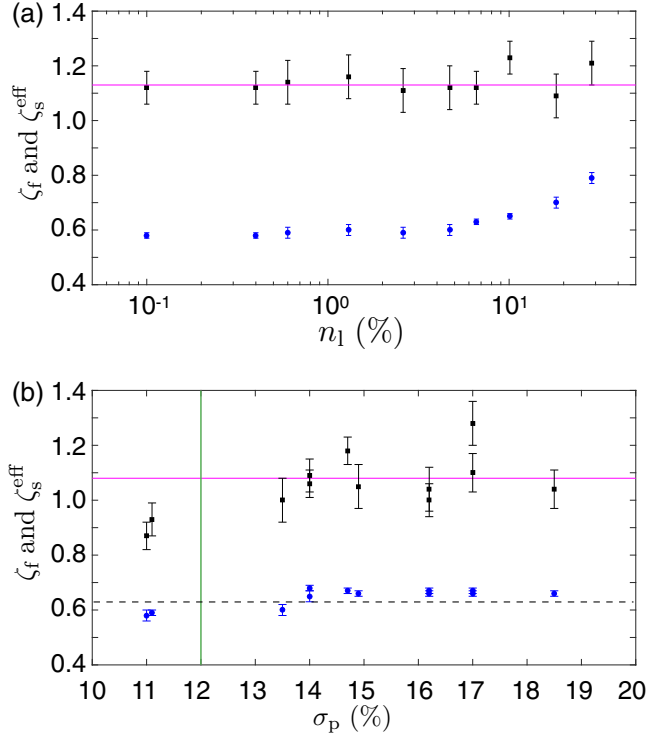


FIG. 7. Freezing-point (●) and the corresponding value of ζ_s^{eff} (■) for (a) b-samples vs the number-fraction of large particles, n_l , and (b) p-samples vs the polydispersity σ_p . The horizontal solid lines represent the mean value of ζ_s^{eff} . In (b) the dashed horizontal line highlights the increase of ζ_f at $\sigma_p \approx 14\%$, and the vertical line shows the limiting polydispersity for crystallization in hard spheres.

for polydispersities $\sigma_p \gtrsim 14\%$ [see Figs. 5(c) and 7(b)]. To understand this difference, we consider the composition of the p-samples. As schematically shown in Fig. 6(b), the size ratio R_l/R_s of the largest and smallest particles in p-samples is considerably smaller than in b-samples. This implies that the particles have similar bulk moduli, and a high particle concentration is needed to reach the osmotic pressure difference necessary for the deswelling of the largest particles. Crystals may form when sufficient large particles have deswollen, and the final size distribution corresponds to about the black curve in Fig. 6(b). The number of large particles that have to be compressed is represented by the light gray area and is smaller than for a b-sample. This may somewhat reduce the ζ_{tot} needed for particle deswelling for the p- relative to the b-samples. In addition, the ratio of the bulk moduli of large and small particles, K_l/K_s , is expected to decrease with increasing σ_p : While this ratio is about constant in the b-samples, it varies in the p-samples, because the size ratio R_l/R_s increases with σ_p . An increase of σ_p thus implies that the large particles become softer relative to the small ones, which tends to reduce the critical concentration for deswelling. This effect contributes towards preventing the increase of ζ_f . Furthermore, in p-samples, a fraction of the large microgels indicated by the dark gray areas in Fig. 6 can cooperate with the small ones to deswell the largest particles. This effect is negligible in the b-samples, where the fraction of large particles with elastic properties similar to the small

particles is small (dark gray areas in Fig. 6). These effects could all contribute towards keeping ζ_f virtually constant in the p-samples with $\sigma_p \gtrsim 14\%$.

The shift of the freezing point in the p-samples from $\zeta_f = 0.58 \pm 0.02$ up to 0.67 ± 0.04 corresponding to a polydispersity increase from about 13% to 15% [see points above and below the dashed line in Fig. 7(b)] indicates that polydispersity is indeed limiting crystallization and that the deswelling of the largest particles is a prerequisite for crystallization. This can be seen from the data shown in Fig. 7(b): For $\sigma_p < 14\%$, ζ_f is consistent with, or slightly larger than the value in the s-samples. However at higher polydispersities, crystallization is limited by the polydispersity. In this region, we find $\zeta_s^{\text{eff}} = 1.08 \pm 0.09$. As in the b-samples, ζ_s^{eff} is essentially constant and slightly above 1. This indicates that the particles in the light gray area of Fig. 6(b) have to be compressed to a size close to that of the small particles before crystals can occur.

D. Structure factor of bidisperse samples

Due to deswelling, the polydispersity of a microgel suspension decreases. This occurs when ζ_{tot} exceeds a critical value and it affects the phase behavior. We study the behavior of large particles in dense suspensions ($0.5 \lesssim \zeta \lesssim 1$) by measuring structure factors of b- and p-samples using SAXS. In fluid-like samples, the position of the first peak q_{peak} is used to calculate the mean nearest-neighbor distance d_{nn} . In crystalline samples, we observe random hexagonal close packed (rhcp) crystals, as expected from other studies with similar microgels [26,45,54]. We use a model for the corresponding structure factor to get the lattice constant and d_{nn} [55]. The structure factor of rhcp crystals contains Bragg peaks and Bragg rods. The latter are due to random stacking of hexagonal planes and are oriented perpendicular to the hexagonal planes, along the direction of random stacking. Importantly, the value of d_{nn} provides information about the deswelling of the large particles. When the large particles shrink and fit into the structure formed by the small ones, there is no increase in d_{nn} with respect to a sample made of small particles only. The d_{nn} of a b-sample with $n_l = (4.7 \pm 0.5)\%$ versus ζ_{tot} is shown with □ symbols in Fig. 8(a); it agrees with the d_{nn} measured for the s-sample made of the small particles in the bidisperse sample (○ symbols). This indicates that the large particles deswell and do not disturb the structure formed by the small particles. Indeed we find $\zeta_s^{\text{eff}} > 1$ for all the crystalline bidisperse samples, as shown by the vertical line, corresponding to $\zeta_s^{\text{eff}} = 1$, in the same figure. Deswelling of the large particles is, therefore, expected according to our model. We use closed symbols for fully crystalline samples or samples exhibiting fluid-crystal coexistence, and open symbols for samples in fluid or glassy states. The dashed, dash-dotted, and dotted lines are fits to the data for small, large, and mixtures of small and large particles, respectively, using the function $a\zeta^{-1/3}$, with a the nearest-neighbor distance at $\zeta = 1$, which is left as fitting parameter. We obtain a ratio $a/(2R_{\text{SAXS}}) = 0.75 \pm 0.06$ for all s-, b-, and p-samples, which reflects that the particles are compressed at $\zeta = 1$, consistent with the SANS data presented in our earlier work [15].

By comparing the structure factors of the bidisperse and the corresponding monodisperse samples, we confirm that

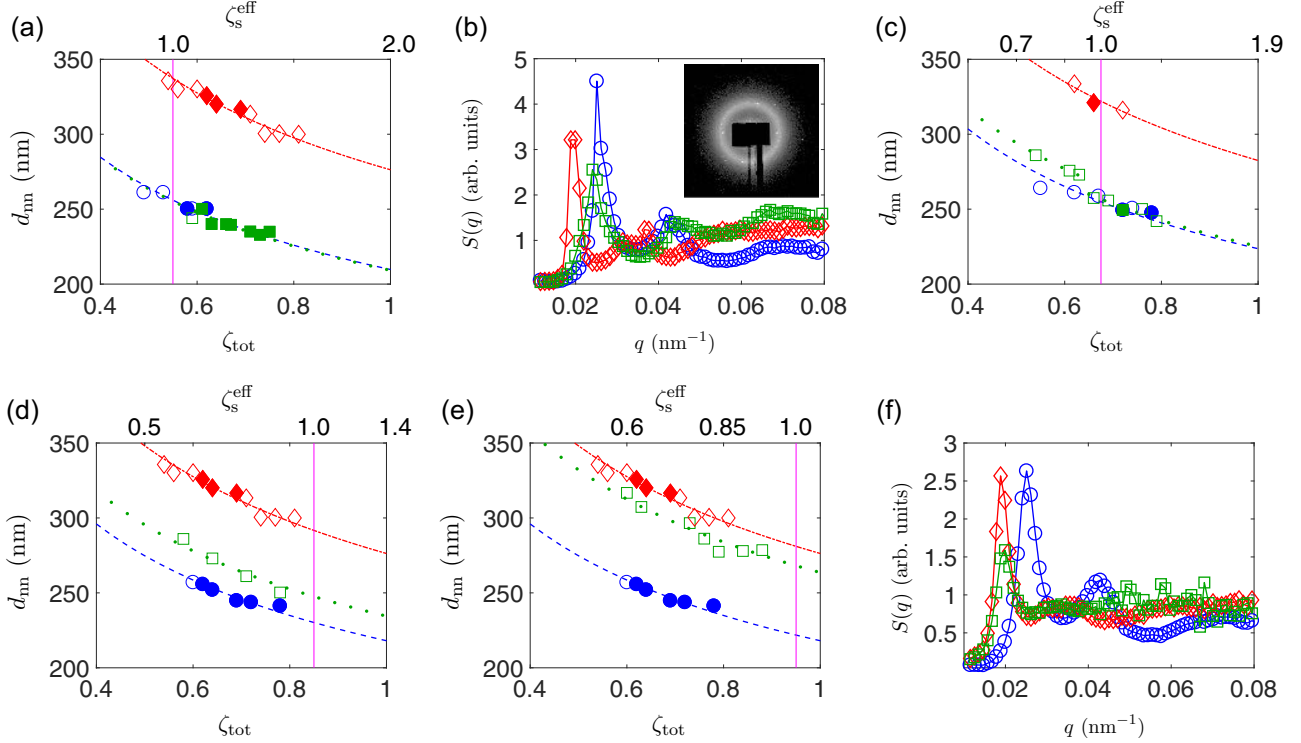


FIG. 8. (a) d_{nn} versus ζ_{tot} for suspensions with small (\circ) and large (\diamond) s-samples as well as the bidisperse b-samples (\square) with $n_1 = (4.7 \pm 0.5)\%$. Solid symbols represent crystalline samples while open symbols represent disordered samples, both fluid and glassy. (b) $S(q)$ of (\square) bidisperse suspension with $n_1 = (18 \pm 2)\%$ and $\zeta = 0.65 \pm 0.02$, (\circ) crystal of s-sample with small particles at $\zeta = 0.62 \pm 0.01$, and (\diamond) crystal of s-sample with large particles at $\zeta = 0.64 \pm 0.02$. The detector image of the bidisperse sample is shown in the inset. (c–e) d_{nn} versus ζ_{tot} with symbols as in (a) and with (c) $n_1 = (29 \pm 3)\%$, (d) $n_1 = (38 \pm 4)\%$, (e) $n_1 = (79 \pm 8)\%$. In panels (a) and (c–e), the effective volume fraction of the small particles, ζ_s^{eff} , is given in the upper x axis. The violet vertical lines correspond to $\zeta_s^{eff} = 1$. The dashed, dotted, and dash-dotted curves show fits to the data with the function $a\zeta^{-1/3}$ for suspensions with small particles only, large particles only, and bidisperse samples, respectively. (f) $S(q)$ of glassy samples: (\square) bidisperse suspension with $n_1 = (79 \pm 8)\%$ and $\zeta = 0.60 \pm 0.02$, (\circ) small s-sample at $\zeta = 0.60 \pm 0.01$, and (\diamond) large s-sample at $\zeta = 0.60 \pm 0.01$. The temperature is fixed to $T = (18.0 \pm 0.5)^\circ\text{C}$ in all measurements.

segregation of large and small particles does not take place in the b-samples; such a comparison for a bidisperse crystalline sample with $n_1 = (18 \pm 2)\%$ is shown in Fig. 8(b). The positions of all Bragg peaks of the bidisperse sample (\square symbols) agree with those of the sample made of only small particles (\circ symbols). No peaks due to crystals of large particles are detected. This confirms that the large particles are compressed and fit into the crystalline lattice formed by the small microgels, consistent with the real-space imaging observations in Ref. [7].

For the sample with $n_1 = (29 \pm 3)\%$, we identify two regions in the behavior of d_{nn} : For $\zeta \gtrsim 0.67$, the nearest-neighbor distance of the bidisperse suspension (\square) virtually coincides with that of the small monodisperse particles (\circ), as shown in Fig. 8(c). However, for $\zeta \lesssim 0.67$, the nearest-neighbor distance of the bidisperse suspension is larger than that of the suspensions with only small particles, indicating that the large particles are not or only partially deswollen, as highlighted by the green dotted line above the blue dashed line. For this sample, the value of ζ_{tot} separating the region where there is overlap in d_{nn} from the region without this overlap corresponds to $\zeta_s^{eff} \approx 1$, as shown by a vertical line in Fig. 8(c) [15].

Increasing n_1 to $(38 \pm 4)\%$ [Fig. 8(d)], and $(79 \pm 8)\%$ [Fig. 8(e)], causes d_{nn} in the b-samples to always be above that of the small s-sample suspensions. This shows that the

large microgels are not or only partially compressed. The $S(q)$ of the sample with $n_1 = (79 \pm 8)\%$, shown in Fig. 8(f), also confirms our interpretation of the data; the position of the first peak of the bidisperse $S(q)$ (\square symbols) coincides with that of the sample made of large particles only (\diamond symbols). The large particles do not deswell, since $\zeta_s^{eff} < 1$ in the considered ζ_{tot} range; the vertical line in Figs. 8(d) and 8(e), corresponding to $\zeta_s^{eff} = 1$, is always above any of the ζ_{tot} values considered. The osmotic pressure difference necessary for deswelling the large particles has thus not been reached.

E. Structure factor of polydisperse samples

The SAXS data of representative p-samples are shown with \square symbols in Figs. 9(a)–9(d) for $\sigma_p = (14.0 \pm 0.8)\%$, $(14.9 \pm 0.1)\%$, $(14.7 \pm 0.8)\%$ and $(13.5 \pm 0.8)\%$. The behavior is similar to that found in the b-samples, except that in these polydisperse samples the nearest-neighbor distance is above the value obtained for the s-sample comprising the smallest particles (\circ symbols) and below the value obtained for the s-sample comprising the largest particles (\diamond symbols). This suggests that the large particles in our p-samples deswell but do not reach the size of the small ones. Compared to the b-samples, where the particles have a large size difference and

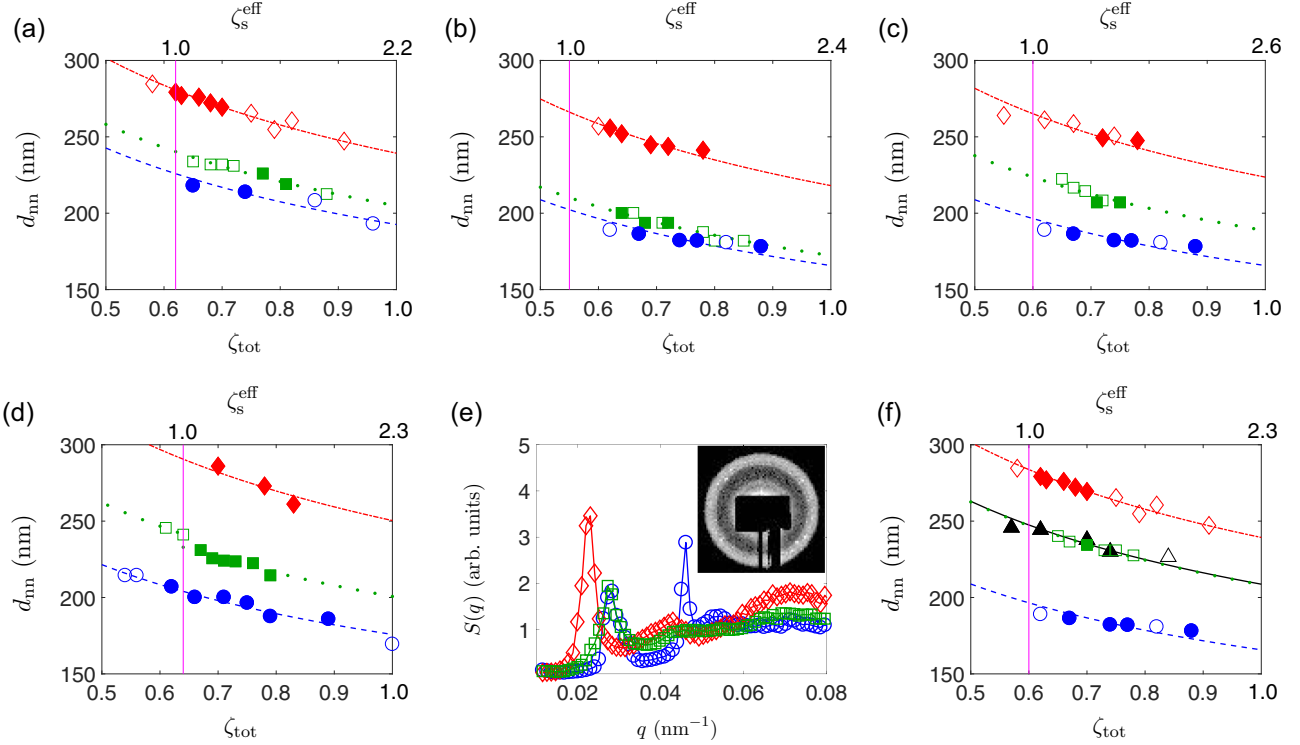


FIG. 9. (a–d) d_{nn} versus ζ_{tot} for suspensions with (○) small and (◇) large s-samples as well as the (□) polydisperse p-samples with (a) $\sigma_p = (14.0 \pm 0.8)\%$, (b) $\sigma_p = (14.9 \pm 0.1)\%$, (c) $(14.7 \pm 0.8)\%$, and (d) $(13.5 \pm 0.8)\%$. (e) $S(q)$ of (□) p-sample with $\sigma_p = (14.9 \pm 0.1)\%$ and $\zeta = 0.64 \pm 0.01$, (○) crystal of only small monodisperse particles at $\zeta = 0.67 \pm 0.02$, and (◇) crystal of only large monodisperse particles at $\zeta = 0.64 \pm 0.02$. In the inset of (e), we show the detector image of the polydisperse sample. (f) d_{nn} versus ζ_{tot} for $\sigma_p = (17 \pm 1)\%$ and with symbols as in (a–d). \triangle symbols represent the third s-sample involved in the p-sample. (a–d and f) Solid symbols represent crystalline samples, while open symbols represent disordered samples, both fluid and glassy. The vertical violet lines correspond to $\zeta_s^{\text{eff}} = 1$. The dashed, dotted, and dash-dotted curves show fits to the data with the function $a\zeta^{-1/3}$, for suspensions comprised of small and large particles, and polydisperse suspensions, respectively. The temperature is fixed to $T = (18.0 \pm 0.5)^\circ\text{C}$ in all measurements.

hence a large difference in bulk modulus, the size difference and hence the difference in bulk modulus is small in the p-samples. This could imply that in these samples the large particles do not need to deswell as much as they do in the b-samples for crystallization to occur. Crystalline samples, shown with solid symbols, are only observed in the ζ -range with $\zeta_s^{\text{eff}} \gtrsim 1$, as indicated by the vertical line at $\zeta_s^{\text{eff}} = 1$ in panels (a–d) and (f). In this range, our model predicts the largest particles to deswell such that crystals can occur.

As in the b-samples, we exclude segregation of small and large particles by comparing the structure factors of the p-samples with those of the samples containing only small or large particles. This is shown in Fig. 9(e) for a p-sample with $\sigma_p = (14.9 \pm 0.1)\%$ (□ symbols). The peak at $q \approx 0.027 \text{ nm}^{-1}$ of the p-sample coincides with the corresponding peak of the s-sample with small particles (○ symbols); no peaks due to a lattice of large particles are detected. In contrast to the s-sample with small particles (○ symbols), the structure factor of the p-sample (□ symbols) has a weak second order reflection and the higher order reflections are not visible. This must reflect an increased disorder in the p-sample. A similar effect has been observed for hard spheres with a highly skewed size distribution, where the absence of higher order reflections was attributed to the large number of defects within the crystallites [50]. For all the studied b- and p-samples, we find the p-samples to have weaker second order reflections than the b-

samples and, therefore, we expect crystals in the p-samples to have more defects than those in the b-samples.

Figure 9(f) shows the d_{nn} of a sample with $\sigma_p = (17 \pm 1)\%$ (□ symbols). This p-sample is composed of three s-samples with small (○ symbols), medium (\triangle symbols), and large (◇ symbols) size particles. As the d_{nn} of the p-sample virtually coincides with that of the medium size sample (\triangle symbols), mainly the large s-particles (◇ symbols) are deswollen. Therefore, we calculate ζ_s^{eff} from the effective sizes of both small (○ symbols) and medium (\triangle symbols) s-samples. As expected, we find crystalline p-samples only in the region with $\zeta_s^{\text{eff}} > 1$.

F. Discussion

As the bulk modulus of microgel particles decreases with increasing particle size, the largest particles in bidisperse or polydisperse suspensions deswell first [7,15], limiting their disturbing effect for crystallization. If the volume fraction after particle deswelling is below the glass transition and the polydispersity is sufficiently low, crystals can form. The freezing point, ζ_f , necessarily appears at a concentration higher than the onset of particle deswelling and is limited by the deswelling mechanism.

Once a narrow size distribution is reached due to deswelling of the largest particles, p- and b-samples show the phase behavior of more monodisperse pNIPAM microgels [22,46,56]

but with freezing and melting points shifted to higher concentration. Also, the observed crystals are compatible with the rhcp structure observed in more monodisperse microgel suspensions [26,45,54]. However, the disorder in the crystal appears to increase.

In samples composed of particles with quite different bulk moduli, as in the b-samples, ζ_f is clearly shifted towards higher ζ with increasing n_1 : With more large particles to be compressed, a larger volume is freed by the deswelling of the large particles and, therefore, a higher concentration is needed to reach the osmotic pressure difference necessary for deswelling. We find that the freezing point shifts up to $\zeta_f \approx 0.79$ at $n_1 = 29 \pm 3\%$ and crystallization does not take place for number fractions of large particles $n_1 \gtrsim 30\%$. The suppression of crystallization may be due to the true volume fraction at the freezing point, ϕ_f , taking particle deswelling into account, increasing above the glass transition for $n_1 \gtrsim 30\%$. In addition, the isotropic compression of the large spheres is expected to be hindered when n_1 increases and most of the large particles have large neighboring particles: While a single large particle surrounded by small particles is expected to remain about spherical when it deswells, a small number of large particles in direct contact may behave differently. As the large particles are softer than the surrounding small ones, the large particles may deform and become anisotropic as they form facets with neighboring large particles when they are compressed [57]. Such deformed large particles in direct contact may hinder crystallization, explaining the observed increase in crystallization time in b- and p-samples, and may contribute to the suppression of crystallization for $n_1 \gtrsim 30\%$. More experimental work, however, is needed to clarify the suppression of crystallization at high n_1 .

When we mix particles with similar size and bulk moduli, as in the p-samples, the effect on the freezing point is strong for $\sigma_p \lesssim 14\%$, as ζ_f shifts from 0.58 to 0.67 with σ_p increasing from 13% to 14%. For higher polydispersities, however, we find the freezing point to remain at $\zeta_f \approx 0.67$ virtually independent of σ_p , until crystallization is suppressed at $\sigma_p \gtrsim 18.5\%$. For polydispersities in the range from 13% to 14%, the polydispersity of the fully swollen particles becomes limiting for crystallization and, with increasing σ_p , deswelling of the large particles becomes a prerequisite for crystallization and causes ζ_f to shift up to $\zeta_f \approx 0.67$, as shown in Fig. 5(c). In the p-samples, the size ratio of largest and smallest particles, R_l/R_s , is significantly lower than in the bidisperse b-samples, and the largest particles are only slightly softer than the small particles. Therefore, one would expect a distinctive shift of the freezing point, as a high $\Delta\Pi$ and ζ_{tot} are required for the deswelling of the largest particles. For σ_p increasing above 14%, we find that (1) the number of large particles that have to deswell for crystallization increases and (2) these large particles become softer relative to the small particles, as the size ratio of large and small particles, R_l/R_s , increases. These two effects appear to cancel each other and, as a consequence, the freezing point remains virtually unchanged. The fluid-crystal coexistence regime appears to become very narrow, and we cannot resolve it for $\sigma_p > 14\%$ within the accuracy of our concentration series. A narrowing of the coexistence region with increasing σ_p is also observed in hard spheres [2]. We find crystallization to be suppressed for $\sigma_p \gtrsim 18.5\%$. In the p-samples, the largest

particles appear to deswell to a size somewhat larger than that of the smaller s-particles, as shown by our SAXS results in Fig. 9, where the p-sample data (\square) always appear above the s-sample data with smaller particles (\circ). Therefore, the polydispersity may be growing with increasing σ_p in spite of the selective deswelling. As for the b-samples, more work is needed to clarify the reason for the suppression of crystallization at high σ_p .

In the literature, the phase behavior and the interaction of soft spheres is modeled with different potentials. Monte Carlo (MC) simulations of monodisperse particles interacting with soft sphere interactions find the freezing point at higher concentrations and a narrower fluid-crystal coexistence region compared to the hard-sphere system. In addition, they also find formation of body-centered cubic (bcc) crystals for polydispersities lower than 12% [58,59], and an inhomogeneous, disordered solid phase coexisting with face-centered cubic (fcc) crystals at higher polydispersities [60]. The Hertzian potential applies to deformable particles. To the best of our knowledge, there are no studies of polydisperse spheres interacting with the Hertzian potential, but in monodisperse, Hertzian spheres [61], several re-entrant melting and first-order transitions between fcc, bcc, hexagonal, simple cubic, body-centered tetragonal, and trigonal crystalline structures have been predicted. A transition from loose fcc to bcc to compressed fcc has been found in a MC simulation study of spheres with a smooth potential with a repulsive shoulder and an attractive well [62]. In addition, by tuning either the depth of the attractive well or the length of repulsion, several other crystalline structures are expected: The simple cubic, face-centered tetrahedral, and hexagonal lattice. A rather general model of soft polymer particles interacting like polymer brushes and minimizing their contact area [63,64] predicts the appearance of bcc crystals in between a low- and a high-density fcc phase. Consistent with this, there is experimental evidence for bcc and fcc-rhcp crystals [11,45].

Theoretical treatments of soft particles reported in the literature include interpenetration or small deformations of the particles, but the spontaneous and selective particle deswelling above a critical concentration that we find seems to control the phase behavior in polydisperse suspensions, is not taken into account. We expect that the osmotic pressure due to counterions and the particle deswelling presented here and in our previous work [15], will allow for reliable modeling of the phase behavior of pNIPAM particles and other microgels. Here we study the behavior of polydisperse suspensions, but the percolation of counterion clouds and the particle deswelling mechanism is also relevant in the monodisperse case.

Our results illustrate that the role of polydispersity changes in microgels with respect to hard spheres and other incompressible particles. The key to this is the inherent compressibility of the particles. Hence, size polydispersity together with the possibility of deswelling the softest particles in the system, which are also the largest, enables crystallization in situations where it would otherwise be hindered. We find that pNIPAM suspensions with a polydispersity up to 18.5% can crystallize without particle segregation. In contrast, hard spheres do not crystallize at polydispersities above 12%, and monocrystals have a polydispersity lower than 5.7% due to particle segregation [1–3].

IV. CONCLUSIONS

Building on our previous study of particle deswelling in concentrated pNIPAM suspensions [15], we find that particle deswelling has a strong effect on the phase behavior of these microgels, in particular on the fluid-crystal transition. As the softness of pNIPAM microgels increases with their size, if they are synthesized according to the same protocol, the largest particles deswell first as the concentration is increased. As a consequence, size polydispersity is reduced as soon as particle deswelling occurs. This spontaneous deswelling allows for crystallization in suspensions with high polydispersity or bidisperse size distributions that would otherwise not crystallize.

As we show in this work, selective deswelling of the largest particles fundamentally changes the role of polydispersity in pNIPAM suspensions compared to hard spheres and other systems comprised of incompressible particles. When the suspension concentration and osmotic pressure are sufficient for particle deswelling, polydispersity is reduced, and the suspension shows the phase behavior of a relatively monodisperse suspension with freezing and melting points shifted to higher concentrations compared to monodisperse suspensions. In contrast, polydispersity always hinders crystallization in hard spheres [2,3,51,65,66].

Further studies are needed to clarify how the deswelling mechanism affects the kinetics of crystallization. It is expected that the two-step crystallization process identified for

monodisperse hard spheres [67,68] does not apply to microgel suspensions, as the formation of crystal precursors and critical nuclei is expected to directly depend on the deswelling of the largest particles.

As the deswelling mechanism presented in our earlier work [15] generally applies to soft polymer particles, and polydispersity is an inherent property of colloidal suspensions, we expect the effect on the suspension phase behavior presented in this work to apply to other concentrated microgel suspensions and possibly other polymer particles, e.g., the soft, DNA-based particles presented in Ref. [69]. The effect of particle deswelling and thus of the compressibility of the particles must be taken into account when the interactions between microgels are modeled. To the best of our knowledge, the interparticle interactions used up to date to model microgels do not include particle deswelling above a critical concentration and no selective deswelling of the largest particles is included. Additional modeling work including this effect is therefore desirable.

ACKNOWLEDGMENTS

The authors thank the Swiss National Science Foundation (200020_153050) and the NSF (DMR-1609841) for financial support. SAXS data were taken on the cSAXS beamline of the Swiss Light Source, Paul Scherrer Institut, and SANS data were taken on the instruments SANS-I and SANS-II at SINQ, Paul Scherrer Institut.

A.S. and U.G. contributed equally to this work.

-
- [1] D. Frenkel, *Nature (London)* **460**, 465 (2009).
 - [2] D. A. Kofke and P. G. Bolhuis, *Phys. Rev. E* **59**, 618 (1999).
 - [3] S. Auer and D. Frenkel, *Nature (London)* **413**, 711 (2001).
 - [4] S. Martin, G. Bryant, and W. van Megen, *Phys. Rev. E* **67**, 061405 (2003).
 - [5] S. Martin, G. Bryant, and W. van Megen, *Phys. Rev. E* **71**, 021404 (2005).
 - [6] A. Kozina, P. Diaz-Leyva, T. Palberg, and E. Bartsch, *Soft Matter* **10**, 9523 (2014).
 - [7] A. S. J. Iyer and L. A. Lyon, *Angew. Chem., Int. Ed. Engl.* **48**, 4562 (2009).
 - [8] R. Pelton, *Adv. Colloid Interface Sci.* **85**, 1 (2000).
 - [9] M. Stieger, W. Richtering, J. S. Pedersen, and P. Lindner, *J. Chem. Phys.* **120**, 6197 (2004).
 - [10] T. Hoare and R. Pelton, *Macromol.* **37**, 2544 (2004).
 - [11] P. S. Mohanty and W. Richtering, *J. Phys. Chem. B* **112**, 14692 (2008).
 - [12] J. J. Lietor-Santos, B. Sierra-Martin, R. Vavrin, Z. Hu, U. Gasser, and A. Fernandez-Nieves, *Macromolecules* **42**, 6225 (2009).
 - [13] J. J. Lietor-Santos, U. Gasser, R. Vavrin, Z. B. Hu, and A. Fernandez-Nieves, *J. Chem. Phys.* **133**, 034901 (2010).
 - [14] J. J. Lietor-Santos, B. Sierra-Martin, U. Gasser, and A. Fernandez-Nieves, *Soft Matter* **7**, 6370 (2011).
 - [15] A. Scotti, U. Gasser, E. S. Herman, M. Pelaez-Fernandez, L. A. Lyon, and A. Fernandez-Nieves, *Proc. Natl. Acad. Sci. USA* **113**, 5576 (2016).
 - [16] M. Peleaz-Fernandez, A. Souslov, L. A. Lyon, P. M. Goldbart, and A. Fernandez-Nieves, *Phys. Rev. Lett.* **114**, 098303 (2015).
 - [17] R. Borrega, M. Cloitre, I. Betremieux, B. Ernst, and L. Leibler, *Europhys. Lett.* **47**, 729 (1999).
 - [18] H. Senff and W. Richtering, *Colloid Polym. Sci.* **278**, 830 (2000).
 - [19] M. Andersson and S. L. Maunu, *J. Polym. Sci., Part B: Polym. Phys.* **44**, 3305 (2006).
 - [20] R. Pelton and T. Hoare, in *Microgel Suspensions: Fundamentals and Applications*, edited by A. Fernandez-Nieves, H. M. Wyss, J. Mattsson, and D. A. Weitz (Wiley-VCH, Weinheim, 2011), Chap. 1.
 - [21] A. Scotti, W. Liu, J. S. Hyatt, E. S. Herman, H. S. Choi, J. W. Kim, L. A. Lyon, U. Gasser, and A. Fernandez-Nieves, *J. Chem. Phys.* **142**, 234905 (2015).
 - [22] H. Senff and W. Richtering, *J. Chem. Phys.* **111**, 1705 (1999).
 - [23] U. Gasser, J. S. Hyatt, J. J. Lietor-Santos, E. S. Herman, L. A. Lyon, and A. Fernandez-Nieves, *J. Chem. Phys.* **141**, 034901 (2014).
 - [24] M. Destribats, V. Lapeyre, M. Wolfs, E. Sellier, F. Leal-Calderon, V. Ravaine, and V. Schmitt, *Soft Matter* **7**, 7689 (2011).
 - [25] P. S. Mohanty, S. Nöjd, K. van Gruijthuisen, J. J. Crassous, M. Obiols-Rabasa, R. Schweins, A. Stradner, and P. Schurtenberger, *Sci. Rep.* **7**, 1487 (2017).
 - [26] S. B. Debord and L. A. Lyon, *J. Phys. Chem. B* **107**, 2927 (2003).
 - [27] S. Schmidt, M. Zeiser, T. Hellweg, C. Duschl, A. Fery, and H. Möhwald, *Adv. Funct. Mater.* **20**, 3235 (2010).

- [28] P. Voudouris, D. Florea, P. van der Schoot, and H. M. Wyss, *Soft Matter* **9**, 7158 (2013).
- [29] L. Zhang, E. S. Daniels, V. L. Dimonie, and A. Klein, *J. Appl. Polym. Sci.* **118**, 2502 (2010).
- [30] G. Romeo, L. Imperiali, J. W. Kim, A. Fernandez-Nieves, and D. A. Weitz, *J. Chem. Phys.* **136**, 124905 (2012).
- [31] D. E. Koppel, *J. Chem. Phys.* **57**, 4814 (1972).
- [32] B. J. Frisken, *Appl. Opt.* **40**, 4087 (2001).
- [33] S. W. Provencher, *Makromol. Chem.* **180**, 201 (1979).
- [34] S. W. Provencher, *Comput. Phys. Commun.* **27**, 213 (1982).
- [35] X. Wu, R. H. Pelton, A. E. Hamielec, D. R. Woods, and W. McPhee, *Colloid Polym. Sci.* **272**, 467 (1994).
- [36] M. Stieger, J. S. Pedersen, P. Lindner, and W. Richtering, *Langmuir* **20**, 7283 (2004).
- [37] G. Romeo, A. Fernandez-Nieves, H. M. Wyss, D. Acierno, and D. A. Weitz, *Adv. Mater.* **22**, 3441 (2010).
- [38] G. K. Batchelor, *J. Fluid Mech.* **83**, 97 (1977).
- [39] K. Kratz, T. Hellweg, and W. Eimer, *Polymer* **42**, 6631 (2001).
- [40] A. Fernandez-Barbero, A. Fernandez-Nieves, I. Grillo, and E. López-Cabarcos, *Phys. Rev. E* **66**, 051803 (2002).
- [41] S. V. Ghugare, E. Chiessi, R. Fink, Y. Gerelli, A. Scotti, A. Deriu, G. Carrot, and G. Paradossi, *Macromolecules* **44**, 4470 (2011).
- [42] J. S. Pedersen, D. Posselt, and K. Mortensen, *J. Appl. Crystallogr.* **23**, 321 (1990).
- [43] B. Hammouda and D. F. R. Mildner, *J. Appl. Crystallogr.* **40**, 250 (2007).
- [44] B. Henrich, A. Bergamaschi, C. Broennimann, R. Dinapoli, E. F. Eikenberry, I. Johnson, M. Kobas, P. Kraft, A. Mozzanica, and B. Schmitt, *Nucl. Instrum. Methods Phys. Res. A* **607**, 247 (2009).
- [45] U. Gasser, J. J. Lieter-Santos, A. Scotti, O. Bunk, A. Menzel, and A. Fernandez-Nieves, *Phys. Rev. E* **88**, 052308 (2013).
- [46] D. Paloli, P. S. Mohanty, J. J. Crassous, E. Zaccarelli, and P. Schurtenberger, *Soft Matter* **9**, 3000 (2013).
- [47] W. G. Hoover and F. H. Ree, *J. Chem. Phys.* **49**, 3609 (1968).
- [48] P. N. Pusey and W. van Megen, *Nature (London)* **320**, 340 (1986).
- [49] S. E. Phan, W. B. Russel, J. Zhu, and P. M. Chaikin, *J. Chem. Phys.* **108**, 9789 (1998).
- [50] S. Martin, G. Bryant, and W. van Megen, *Phys. Rev. Lett.* **90**, 255702 (2003).
- [51] H. J. Schöpe, G. Bryant, and W. van Megen, *Phys. Rev. E* **74**, 060401 (2006).
- [52] B. Sierra-Martin, J. J. Lieter-Santos, A. Fernandez-Barbero, T. T. Nguyen, and A. Fernandez-Nieves, in *Microgel Suspensions: Fundamentals and Applications*, edited by A. Fernandez-Nieves, H. M. Wyss, J. Mattsson, and D. A. Weitz (Wiley-VCH, Weinheim, 2011), Chap. 4.
- [53] R. Piazza, S. Buzzacco, and E. Secchi, *J. Phys.: Condens. Matter* **24**, 284109 (2012).
- [54] J. Brijitta, B. V. R. Tata, R. G. Joshi, and T. Kaliyappan, *J. Chem. Phys.* **131**, 074904 (2009).
- [55] W. Loose and B. J. Ackerson, *J. Chem. Phys.* **101**, 7211 (1994).
- [56] T. Hellweg, C. D. Dewhurst, E. Brückner, K. Kratz, and W. Eimer, *Colloid Polym. Sci.* **278**, 972 (2000).
- [57] M. Cloitre, R. Borrega, F. Monti, and L. Leibler, *C. R. Phys.* **4**, 221 (2003).
- [58] W. G. Hoover, S. G. Gray, and K. W. Johnson, *J. Chem. Phys.* **55**, 1128 (1971).
- [59] R. Agrawal and D. A. Kofke, *Mol. Phys.* **85**, 23 (1995).
- [60] L. A. Fernandez, V. Martin-Mayor, and P. Verrocchio, *Phys. Rev. Lett.* **98**, 085702 (2007).
- [61] J. C. Pàmies, A. Cacciuto, and D. Frenkel, *J. Chem. Phys.* **131**, 044514 (2009).
- [62] Y. D. Fomin, E. N. Tsiok, and V. N. Ryzhov, *J. Chem. Phys.* **134**, 044523 (2011).
- [63] P. Ziherl and R. D. Kamien, *Phys. Rev. Lett.* **85**, 3528 (2000).
- [64] P. Ziherl and R. D. Kamien, *J. Phys. Chem. B* **105**, 10147 (2001).
- [65] U. Gasser, *J. Phys.: Condens. Matter* **21**, 203101 (2009).
- [66] T. Palberg, *J. Phys.: Condens. Matter* **26**, 333101 (2014).
- [67] H. J. Schöpe, G. Bryant, and W. van Megen, *Phys. Rev. Lett.* **96**, 175701 (2006).
- [68] S. Golde, T. Palberg, and H. J. Schöpe, *Nat. Phys.* **12**, 712 (2016).
- [69] J. Zhang, P. M. Lettinga, J. K. G. Dhont, and E. Stiakakis, *Phys. Rev. Lett.* **113**, 268303 (2014).